

Study of an electro-optic modulator capable of generating simultaneous amplitude and phase modulations

Benedict J Cusack, Benjamin S Sheard, Daniel A Shaddock *, Malcolm B Gray and Ping Koy Lam
*Department of Physics and Theoretical Physics, Faculty of Science,
The Australian National University, Canberra ACT 0200, Australia*

Stan E Whitcomb
LIGO Laboratory, MS 18-34, California Institute of Technology, Pasadena CA, USA
(Dated: Friday, 8th August, 2003)

We report on the analysis and prototype-characterization of a dual-electrode electro-optic modulator that can generate both amplitude and phase modulations with a selectable relative phase, termed a *universally tunable modulator* (UTM). All modulation states can be reached by tuning only the electrical inputs, facilitating real-time tuning, and the device is shown to have good suppression and stability properties. A mathematical analysis is presented, including the development of a geometric phase representation for modulation. The experimental characterization of the device shows that relative suppressions of 38 dB, 39 dB and 30 dB for phase, single-sideband and carrier-suppressed modulations, respectively, can be obtained, as well as showing the device is well-behaved when scanning continuously through the parameter space of modulations. Uses for the device are discussed, including the tuning of lock points in optical locking schemes, single sideband applications, modulation fast-switching applications, and applications requiring combined modulations.

PACS numbers:

I. INTRODUCTION

Although electro-optic amplitude modulators and phase modulators are commonplace in modern optics laboratories, there is no single, commercially available device that produces controllable amplitude and phase modulations with complete variability. When required, various optical configurations have been assembled, such as phase and amplitude modulators in series [1], and two phase modulators used in a Mach-Zehnder interferometric setup (the Mach-Zehnder modulator) [2], which are both capable of amplitude and phase modulation.

The device discussed in this paper, called a *universally tunable modulator* (UTM), is a modification of a commercial electro-optic amplitude modulator. An amplitude modulator consists of two phase-modulation crystals aligned at right angles, and connected with opposite polarities to a single electrical input. A UTM (see Fig. 1(a)) is identical, but with two separate inputs, one connected to each crystal. A prototype was constructed from a New Focus broadband amplitude modulator (Model 4104) in this way. We demonstrate here that this extra degree of freedom enables the production of phase as well as amplitude modulation.

We use the term "universally tunable" to highlight the fact that the device is capable of both amplitude modulation (AM) and phase modulation (PM), with full selectability of the amplitude of each and of the relative phase between the two. Choosing a figure of merit with

which to assess the device is difficult in general, and depends on the modulation requirements of the application in question. We address this issue here by identifying two characteristics that might be expected of the modulation states produced by the device: *variability* and *purity*. The variable nature of the device is brought out by experiments which require real-time tuning of the modulator across its parameter space. Other experiments rely on precise selection of a small number of operating points, where the purity of the modulations produced has a direct influence on the success of the experiment.

One anticipated use for the UTM device is in optical feedback control of the resonance condition of a Fabry-Perot cavity, or the fringe condition of a Michelson interferometer. The RF modulation techniques used to lock these devices are Pound-Drever-Hall locking [3] and Schnupp modulation locking [4], respectively, and are both based on properties of the devices that convert (injected) PM to AM, which is then demodulated to give an error signal readout. In both cases, the default locking point is at a turning point in the transmitted (or reflected) optical field intensity; injection into the device of additional AM (along with the default PM) causes the device to lock with an offset relative to the turning point. Moreover, the quadrature of AM required for Pound-Drever-Hall locking is orthogonal to that required for Schnupp modulation locking, introducing the possibility of independently tuning two lock points at once in a coupled system. This *RF offset locking* application is our case study example to demonstrate the variability property of a prototype UTM; the technique may be useful for future large-scale gravitational wave detector configurations [5], with the feature of facilitating real-time tuning of detector frequency responses [6, 7, 8].

*Daniel Shaddock is currently employed at the Jet Propulsion Laboratory, Pasadena CA, USA.

The UTM device is capable of several "pure" states, which have various applications as well as providing a natural way to test the purity property of the prototype. Single-sideband modulation, for example, requires an equal combination of AM and PM, in quadrature. The subject has arisen a number of times with optic fibre technology where, for example, a single-sideband-modulated signal is immune to fibre dispersion penalties [2], and the technique has also been suggested for subcarrier-multiplexing systems [9]. Single-sideband modulation has been achieved by other means: optically filtering out one sideband [10]; cascaded amplitude and phase modulators [1]; Mach-Zehnder modulators [2]; and more complex arrangements [11]. While these methods have merit, we submit that the UTM is far simpler in design, with fewer degrees of freedom available to drift, and is at least comparable regarding suppression capabilities.

The UTM can produce PM or AM states, with purity limited by the accuracy of polarisation optics (including the birefringent effects of the device itself). While these states are obtainable using off-the-shelf amplitude or phase modulators, applications in coherent state quantum cryptography require fast-switching between AM and PM [12], for which the UTM is ideal. Other applications, including some quantum communication protocols [13], would also benefit from having easy access to a tuned, stationary combination of AM and PM. In addition, we show that the UTM (or indeed an amplitude modulator) can produce a *carrier suppression* state, where the output consists only of two modulation sidebands.

We have developed a geometric phase sphere description of modulation states, the *modulation sphere* formulation, in analogy with the Poincaré sphere description for polarisation states [14]. We demonstrate the use of this formalism by calculating the transfer function (electrical to optical) of the UTM device, both using optical-field-phasors and using modulation sphere parameters, and discuss the pros and cons of the two mathematical descriptions. We have found that the modulation sphere representation is particularly useful for gaining a visual insight into the dynamics of the UTM.

Section II gives the mathematical description of the UTM, in terms of optical-field-phasors (Section II B), and the modulation sphere formulation (Section II C). The transfer functions from these two subsections are derived in Appendices A 1 and A 2 respectively. Section III describes a characterisation experiment conducted on a prototype UTM, with the experimental layout described in Section III B, and the results presented in Section III C. The main results of the study are summarised in Section IV.

II. THEORETICAL MODEL

A. Overview

Before we proceed, a simple analogy may help to clarify the inner workings of a UTM device, and lend physical insight. A Mach-Zehnder modulator involves splitting a beam into two parts, separately phase-modulating each part, then recombining the two parts on a beamsplitter. The UTM is physically equivalent to this, where the two interferometer paths are collinear but different in polarisation. Each UTM crystal modulates one and only one polarisation component. The phase between the electric fields in the two polarisation states we identify as the interferometric recombination phase. The birefringent waveplates used to create the initial polarisation take the place of the input beamsplitter, and a polarising beamsplitter facilitates the output recombination. The recombination phase is adjustable (by modifying the polarisation state), and one can control the amplitudes and phases of the single-beam phase-modulations generated by each of the two crystals. Through manipulation of these input parameters, the user has complete control over the interference condition of the two carrier beams, and separately over the interference of the lower and upper sidebands generated by the modulating crystals. This amounts to having complete freedom to choose any modulation state by appropriate choice of the input parameters.

As an example, consider two identically phase-modulated beams, where the optical phase of one beam is advanced by 90° , and the modulation phase of the other beam is advanced by 90° . The result, upon interfering the two beams, is that one resultant sideband is exactly cancelled out and the other is additively reinforced, producing a single sideband state. One can intuitively arrive at all of the modulation states discussed in this paper by reasoning along these lines. In the next section, we quantify such reasoning into a mathematical theory of the UTM.

B. UTM Transfer Function

As stated earlier, a UTM (see Fig. 1(a)) consists of two modulating crystals in series, with separate voltage sources, and with modulating axes at right angles to each other. The UTM is used by sending a laser beam of elliptical polarisation through the system, and then through a linearly polarising filter angled at 45° to the crystals' modulating axes.

The choice of polarisation state of the incident beam has a crucial effect on the transfer characteristics of the system. We will restrict ourselves to a subset of polarisation states: those where there is equal power in the polarisation components aligned with each modulating crystal axis. Equivalently, we require that the polarisation is elliptical with major and minor axes aligned at 45°

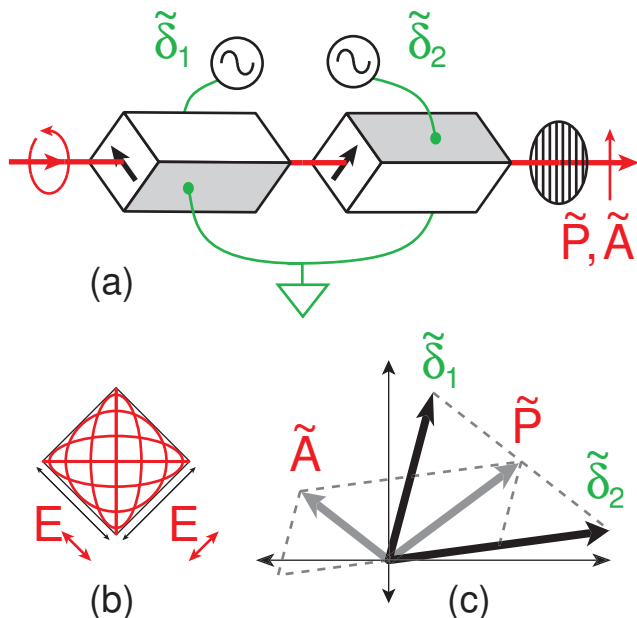


FIG. 1: (a) UTM schematic. Two modulating crystals are positioned in series with modulating axes at 90° . A laser beam of elliptical polarisation passes through each crystal and then through a vertically polarising element. (b) The subset of input beam polarisation states considered here is all states such that there is an equal optical field amplitude in both the left- and right-diagonal components. σ equals the phase between these components: shown are $\sigma = 0$ (vertical), $\pi/4$, $\pi/2$ (circular), $3\pi/4$, and π (horizontal). (c) Phasor diagram representing the transfer function given by Eq. 3. If the input electrical signals are represented as rotating phasors ($\tilde{\delta}_1$ and $\tilde{\delta}_2$), then the corresponding phasors that represent the output phase and amplitude modulations (\tilde{P} and \tilde{A}) are proportional to their sum and difference respectively.

to both crystal axes. For concreteness we will choose the ellipse axes to be horizontal and vertical, and the crystal axes to be left and right diagonal (as in Fig. 1(a)). We define the angle σ as being the phase difference between left-diagonal and right-diagonal electric field components of the light exiting the crystals (see Fig. 1(b)). The identity

$$\tan^2\left(\frac{\sigma}{2}\right) = \frac{P_h}{P_v} \quad (1)$$

follows, where $P_{h,v}$ are the powers in the horizontal and vertical polarisation components of the input laser beam. We introduce this degree of freedom with the application of gravitational wave detector locking schemes in mind, where laser power is at a premium: choosing σ such that the beam is almost vertically polarised allows us to retain the majority of the input carrier power, while retaining full access to all modulation states, albeit with reduced amplitude.

Note that, in the ideal situation where both crystals have identical refractive indices and lengths, the phase angle σ (and hence the polarisation state) is the same before and after the modulator. However, a real device

almost certainly does not have identical crystals so that the relative phase between left- and right-diagonal components may well be changed by the crystals, in which case σ should describe the polarisation state of the light *exiting* the modulator, just before it reaches the linearly polarising filter.

The inputs to the two crystal electrodes are sinusoidal voltages of frequency ω_m ; we describe these as complex phasors $\tilde{\delta}_j = \delta_j e^{i\phi_j}$ ($j = 1, 2$, and $i = \sqrt{-1}$) so that the single-crystal phase modulations are given by $\Re\{\tilde{\delta}_j e^{i\omega_m t}\} = \delta_j \cos(\omega_m t + \phi_j)$, where \Re and \Im respectively return the real and imaginary components of a complex variable.

We can similarly write the output phase and amplitude modulations as complex phasors $\tilde{P} = P e^{i\phi_P}$ and $\tilde{A} = A e^{i\phi_A}$ where the optical field amplitude exiting the UTM can be shown to be:

$$\begin{aligned} E_{\text{OUT}} &= E_{\text{IN}} \left[\cos(\sigma/2) + i\Re\{\tilde{P}e^{i\omega_m t}\} + \Re\{\tilde{A}e^{i\omega_m t}\} \right] \\ &= E_{\text{IN}} [\cos(\sigma/2) + iP\cos(\omega_m t + \phi_P) + A\cos(\omega_m t + \phi_A)](2) \end{aligned}$$

where E_{IN} is the input optical field amplitude. In Eq. 2, we have assumed small single-crystal modulation depths ($\delta_j \ll 1$), and we have factored away the net optical phase dependence.

The relationship between input and output parameters for the UTM device can be shown to be:

$$\begin{aligned} \tilde{P} &= \frac{1}{2} \cos\left(\frac{\sigma}{2}\right) (\tilde{\delta}_1 + \tilde{\delta}_2) \\ \tilde{A} &= \frac{1}{2} \sin\left(\frac{\sigma}{2}\right) (\tilde{\delta}_1 - \tilde{\delta}_2). \end{aligned} \quad (3)$$

(A proof of this transfer function is outlined in Appendix A 1.)

An important observation from Eq. 3 is that the phases of the AM and PM track the phases of the sum and difference of the electrical signals, respectively. Thus, an electronic oscillator for use in demodulation schemes is readily available, and can be calibrated once for all operating points. This phase-tracking property holds for any choice of σ ; the effect of a change of polarisation ellipticity is to change the overall quantity of PM or AM available (as well as changing the overall beam power in Eq. 2).

Returning briefly to the topic of conserving as much carrier power as possible for gravitational wave detector applications, we derive a useful rule-of-thumb for selecting an appropriate amount of power to tap off. Consider Eq. 3 when we set $\tilde{\delta}_1 = i\tilde{\delta}_2$ such that $\tilde{\delta}_1 + \tilde{\delta}_2$ and $\tilde{\delta}_1 - \tilde{\delta}_2$ have the same magnitude (we do this in order to focus on the *coefficients* of the complex $\tilde{\delta}_j$ phasors). The ratio of modulation power between the AM and PM components is $|\tilde{A}|^2/|\tilde{P}|^2 = \tan^2(\sigma/2)$ and, comparing this with Eq. 1, we have:

$$\frac{|\tilde{A}|^2}{|\tilde{P}|^2} = \frac{P_h}{P_v} \quad (4)$$

So, the fraction of power tapped off is directly proportional to the fraction of modulation power available to be expressed as AM (rather than PM). Typically then, if 10% of the output power is tapped off, and the user wishes to alternately produce a pure PM state and then a pure AM state (each of the same modulation power), then the AM state will require 9 times the input electrical power in compensation, compared to the PM state.

It is apparent from Eqs. 2 and 3 that for $\sigma = \pi$ the carrier and the PM contribution vanish, leaving only the AM component. This is the *carrier suppression* operating point, where only two sidebands remain. The modulation ceases to be of the phase or amplitude type due to the absence of a carrier as a phase reference, though the modulation retains its beat phase through the second harmonic in optical power.

A rearrangement of Eq. 2 serves to clarify the nature of single sideband modulation:

$$E_{\text{OUT}} = E_{\text{IN}} \left[\cos(\sigma/2) + \frac{1}{2} (\tilde{A} + i\tilde{P}) e^{i\omega_m t} + \frac{1}{2} (\tilde{A} - i\tilde{P})^* e^{-i\omega_m t} \right] \quad (5)$$

where the $e^{\pm i\omega_m t}$ terms represent optical sidebands at $\pm\omega_m$ relative to the optical carrier frequency, and an asterisk denotes a complex conjugate. It is clear then that choosing $\tilde{A} = \pm i\tilde{P}$ eliminates one or other of the sidebands. In other words, a single sideband state corresponds to having equal amounts of PM and AM where the two modulations are in quadrature.

C. Modulation Sphere Formulation

We now define a geometric phase representation of the modulation parameters of the system to further clarify the transfer characteristics of the UTM device. This is analogous to using Stokes parameters and the Poincaré sphere representation for optical polarisation states [14]. In this case, we transform from the complex quantities \tilde{P} and \tilde{A} to a set of (real) coordinates (M_1, M_2, M_3) in *M-space* via the transformation:

$$\begin{aligned} M_1 &= P^2 - A^2 \\ M_2 &= 2PA\cos(\phi_P - \phi_A) = 2\Re\{\tilde{P}\tilde{A}^*\} \\ M_3 &= 2PA\sin(\phi_P - \phi_A) = 2\Im\{\tilde{P}\tilde{A}^*\} \end{aligned} \quad (6)$$

A single point in M-space represents a distinct modulation state. In particular, the M-space representation suppresses the common (beat) phase of the modulation state; the equations are defined in terms of the relative phase difference between AM and PM contributions. This is a useful simplification in that now every physically distinct modulation corresponds to one point and one only. On the other hand, one cannot use the representation for demodulation-phase-tracking calculations, when the

physical significance of the modulation's overall phase is

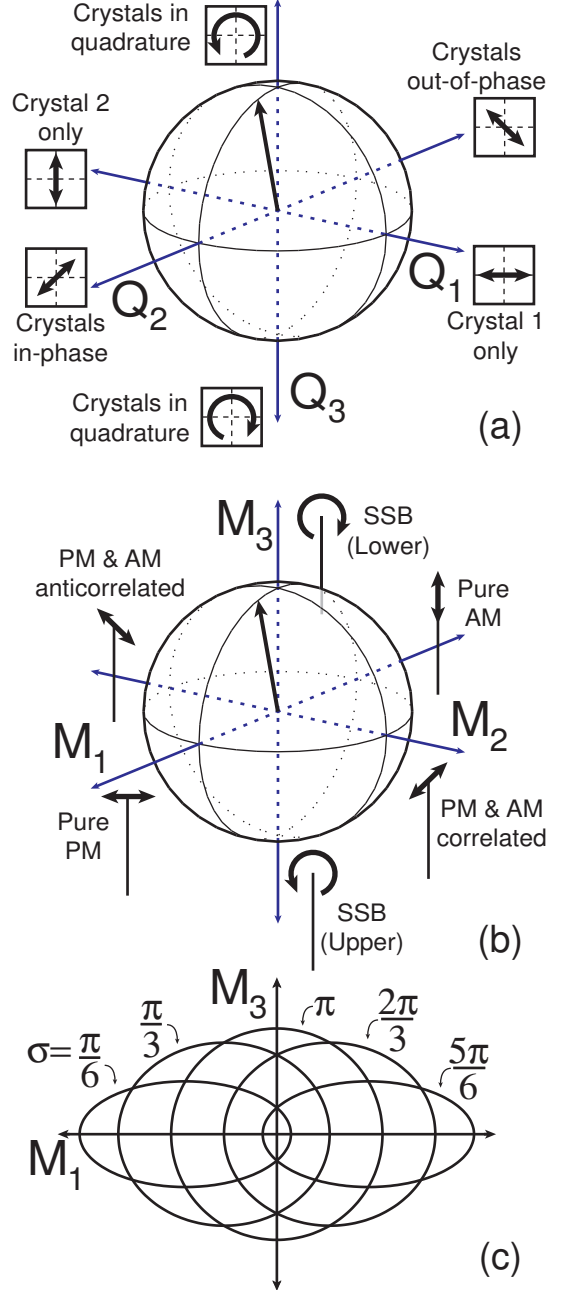


FIG. 2: (a) Q-space diagram. Axis labels are visual reminders of relative amplitudes and phases of input electrical signals (try to visualise the display of a cathode ray oscilloscope run in X-Y mode with δ_1 and δ_2 as the X and Y inputs). (b) M-space diagram. Axis labels are optical amplitude phasors whose endpoints oscillate at the modulation frequency. For $\sigma = \pi/2$, there is a graphical transfer correspondence between (a) and (b) according to Eq. 9. (c) In general, the transfer function of the UTM, Eq. 8, takes a sphere of constant input power in Q-space and returns an ellipse in M-space. A cross section is shown for a selection of values for σ .

renewed by the presence of an external (electrical) phase reference.

Operating point	Modulations	Electrical Inputs	M-space	Q-space
Pure PM	$\tilde{P} \neq 0, \tilde{A} = 0$	$\tilde{\delta}_1 = \tilde{\delta}_2$	$(+M_0, 0, 0)$	$(0, \frac{4M_0}{\cos(\sigma)+1}, 0)$
Pure AM	$\tilde{P} = 0, \tilde{A} \neq 0$	$\tilde{\delta}_1 = \tilde{\delta}_2 e^{i\pi}$	$(-M_0, 0, 0)$	$(0, \frac{4M_0}{\cos(\sigma)-1}, 0)$
Correlated PM & AM	$\tilde{P} = \tilde{A}$	$\tilde{\delta}_1 \cos(\sigma) = \tilde{\delta}_2 e^{i\pi} (1 + \sin(\sigma))$	$(0, +M_0, 0)$	$(\frac{4M_0}{\sin(\sigma)}, -\frac{4M_0 \cos(\sigma)}{\sin^2(\sigma)}, 0)$
Anticorrelated PM & AM	$\tilde{P} = \tilde{A} e^{i\pi}$	$\tilde{\delta}_1 (1 + \sin(\sigma)) = \tilde{\delta}_2 e^{i\pi} \cos(\sigma)$	$(0, -M_0, 0)$	$(-\frac{4M_0}{\sin(\sigma)}, -\frac{4M_0 \cos(\sigma)}{\sin^2(\sigma)}, 0)$
Single sideband $-\omega_m$	$\tilde{P} = \tilde{A} e^{i\pi/2}$	$\tilde{\delta}_1 = \tilde{\delta}_2 e^{i(\pi+\sigma)}$	$(0, 0, +M_0)$	$(0, -\frac{4M_0 \cos(\sigma)}{\sin^2(\sigma)}, -\frac{4M_0}{\sin(\sigma)})$
Single sideband $+\omega_m$	$\tilde{P} = \tilde{A} e^{-i\pi/2}$	$\tilde{\delta}_1 = \tilde{\delta}_2 e^{i(\pi-\sigma)}$	$(0, 0, -M_0)$	$(0, -\frac{4M_0 \cos(\sigma)}{\sin^2(\sigma)}, \frac{4M_0}{\sin(\sigma)})$

TABLE I: Details of significant operating points. The modulation parameters, expressed both in terms of phasors and M-space parameters, are given for each point. The electrical inputs required to produce these operating points are also given (both in terms of phasors and Q-space parameters), and these inputs vary with the polarisation parameter σ .

The three M-space parameters can be interpreted as follows: M_1 measures the extent to which one kind of modulation (AM or PM) dominates over the other; M_2 measures the degree to which the present PM and AM components are correlated or anti-correlated in phase; and M_3 measures the degree to which the present PM and AM components are in quadrature phase to each other, and thus also measures the extent to which one frequency sideband has more power than the other. We also define the *modulation power* by $M_0 = P^2 + A^2$, from whence $M_0^2 = M_1^2 + M_2^2 + M_3^2$ follows. Therefore, a surface of constant M_0 is a sphere in M-space (see Fig. 2(b)).

We attach particular significance to modulation states whose M-space coordinates lie on one cardinal axis. The point $(+M_0, 0, 0)$ represents pure PM, and the point $(-M_0, 0, 0)$ represents pure AM. The points $(0, \pm M_0, 0)$ represent correlated and anti-correlated PM and AM, and $(0, 0, \pm M_0)$ represent upper and lower single sideband states. Details of these states are summarised in Table I. These states, particularly those on the M_1 and M_3 axes, involve the suppression of a particular signal, and so provide a natural way to test the precision of a real device.

Before we proceed, it is convenient to define an analogous *Q-space* representation, (Q_1, Q_2, Q_3) , for the electrical input parameters, via:

$$\begin{aligned}
Q_1 &= \delta_1^2 - \delta_2^2 \\
Q_2 &= 2\delta_1\delta_2\cos(\phi_1 - \phi_2) = 2\Re\{\tilde{\delta}_1\tilde{\delta}_2^*\} \\
Q_3 &= 2\delta_1\delta_2\sin(\phi_1 - \phi_2) = 2\Im\{\tilde{\delta}_1\tilde{\delta}_2^*\}
\end{aligned} \tag{7}$$

where $Q_0 = \delta_1^2 + \delta_2^2 = \sqrt{Q_1^2 + Q_2^2 + Q_3^2}$ is the sum input electrical power. Physical interpretations for these parameters correspond with the M-space equivalents (see Fig. 2(a) for a diagrammatic description).

Now, we can rewrite the UTM transfer function, Eq. 3,

in terms of the M-space and Q-space parameters:

$$\begin{aligned}
M_0 &= \frac{1}{4}(Q_0 + Q_2\cos(\sigma)) \\
M_1 &= \frac{1}{4}(Q_0\cos(\sigma) + Q_2) \\
M_2 &= \frac{1}{4}\sin(\sigma)Q_1 \\
M_3 &= -\frac{1}{4}\sin(\sigma)Q_3
\end{aligned} \tag{8}$$

(A proof of this transfer function is outlined in Appendix A 2.)

Since the modulation power M_0 depends partly on Q_2 (and hence depends on the *detail* of the input signals, not just the overall input power Q_0), a sphere of constant electrical input power in Q-space does *not*, in general, map to a sphere of constant modulation power in M-space. In fact, Eq. 8 describes a transfer function from a sphere in Q-space to an *ellipsoid* in M-space. It can be shown that the ellipsoid is centered at $(M_1, M_2, M_3) = (Q_0\cos(\sigma)/4, 0, 0)$, has radii $[Q_0/4, Q_0\sin(\sigma)/4, Q_0\sin(\sigma)/4]$, and has an eccentricity of $\epsilon = |\cos(\sigma)|$. The ellipse is always prolate with long axis aligned with the M_1 -axis, and always has one focus at the M-space origin. The orthogonality of axes is preserved in the transformation, which consists only of a translation (the ellipsoid is not origin-centered) and a dilation (the ellipsoid is squashed in the M_2 and M_3 directions). The centrepoint and proportions of the ellipsoid are parametrised by the input light's polarisation parameter, σ (see Fig. 2(c)).

A special case occurs for $\sigma = \pi/2$ (circular input polarisation), when Eq. 8 reduces to:

$$\begin{aligned}
M_0 &= \frac{1}{4}Q_0 \\
M_1 &= \frac{1}{4}Q_2 \\
M_2 &= \frac{1}{4}Q_1 \\
M_3 &= -\frac{1}{4}Q_3
\end{aligned} \tag{9}$$

Here, a sphere in Q-space maps to a sphere in M-space. This case is particularly instructive as Figs. 2(a) and 2(b)

baseband via a *double-demodulation* scheme. This gave a DC readout of the PM and AM amplitudes at a selected beat phase. A complete description of the modulation strengths and quadratures was obtained in this way, and was hence useful to characterise the *variability* of the UTM prototype.

The method of signal extraction via double demodulation is best understood by reworking the last two components of Eq. 10 to:

$$P_{\omega_h - \omega_m} + P_{\omega_h + \omega_m} = 2\cos\left(\frac{\sigma}{2}\right) \left[\Re\{\tilde{P}e^{i\omega_m t}\} \Im\{\gamma e^{i\omega_h t}\} + \Re\{\tilde{A}e^{i\omega_m t}\} \Re\{\gamma e^{i\omega_h t}\} \right] \quad (11)$$

This signal is mixed down to base band by demodulating at $\omega_h/2\pi = 80$ MHz and then $\omega_m/2\pi = 5$ MHz in series. The output of a demodulation is sensitive to the relative phases of the signals being mixed: if they are exactly in-phase or out-of-phase, the output will be maximally positive or negative; if they are in quadrature, the output will be zero. Eq. 11 shows that the ω_h oscillator components of the AM and PM portions are orthogonal (one is the real component, the other is imaginary) so that the appropriate choice of electrical oscillator phase can force the readout of PM only, or AM only, or some linear combination of the two. Similarly, the demodulation quadrature of the ω_m stage determines the beat phase that the output signal is projected onto.

The output DC component of the *first* stage of demodulation (extracted with a bias-T component) was used as an error signal for locking the optical recombination phase of the heterodyne. This error signal varies sinusoidally with respect to the optical recombination phase, with a zero crossing where the optical heterodyne beat (P_{ω_h}) and the electronic demodulation oscillator are in quadrature. In other words, the feedback loop "locks out" the heterodyne beat. Comparing Eq. 10 and Eq. 11, we see that the AM term has the same phase as the P_{ω_h} term (that is, they both contain the terms $\Re\{\gamma e^{i\omega_h t}\}$), so that the feedback loop also locks out the AM component of modulation, leaving only the PM component (which has a $\Im\{\gamma e^{i\omega_h t}\}$ term). This is an important part of the process as, without a locking loop, the demodulation phase of the circuit would be uncharacterised, and would also be free to drift.

In the experiment, two separate double demodulation schemes were used in order to measure PM and AM simultaneously; the ω_h signal was split with a 90° electronic splitter to ensure that the two double demodulation circuits scanned orthogonal modulations. Hence, when the heterodyne locking loop was connected using a signal from one double-demodulation circuit, this ensured that that particular circuit was sensitive to PM and that the other was sensitive to AM.

Regarding the second stage of demodulation, electronically phase locking the signal generators was sufficient to time-stabilise the demodulation quadrature, and a known modulation was used for calibration.

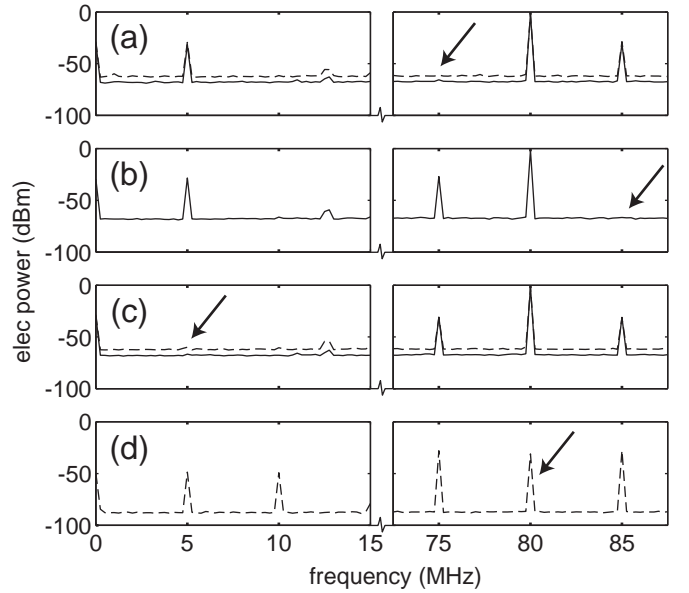


FIG. 4: Spectrum analyser traces of heterodyne measurements of four "pure" operating points. Frequencies of interest are 5 MHz (direct AM beat), 80 MHz (heterodyne-carrier beat), and 75 MHz and 85 MHz (heterodyne-sideband beats). A solid line indicates data averaged over a few seconds, a dotted line indicates max-hold data acquired over approximately an hour, and arrows indicate lines that have been suppressed. The plots are: (a) upper single-sideband (lower sideband suppressed by 34.9 dB); (b) lower single-sideband (upper sideband suppressed by 39.5 dB); (c) pure PM (AM beat suppressed by around 38 dB); (d) carrier suppression (heterodyne beat suppressed by around 30 dB).

C. Results

Fig. 4 shows spectrum analyser traces for four operating points, to demonstrate the suppression capabilities of the device. The suppression factors are 34.9 dB and 39.5 dB for the left- and right-hand sidebands (Fig. 4(a) and Fig. 4(b)). The figures shown suppress the frequency lines down to the electronic noise floor, so that higher suppression factors may be possible. A more detailed trace exhibiting sideband suppression is given in Fig. 5, with 35.2 dB relative suppression recorded.

We measured around 38 dB suppression of the AM beat compared with a similar-input-power pure-AM state (Fig. 4(c)). In this and the other diagrams in Fig. 4, we have shown "max-hold" data, demonstrating that the device is highly stable, maintaining these operating points without significant drift on the timescale of hours.

In Fig. 4(d), the carrier is suppressed by selecting the AM operating point and setting $\sigma = \pi$ (horizontal polarisation). The heterodyne measurement of the carrier is down by around 30 dB, from which we can infer that the carrier power (which goes as the square of the heterodyne measurement) is down by 60 dB. This heterodyne measurement is further supported by observing that the first and second harmonics of direct AM beat are approximately equal, which is consistent with the fact that the

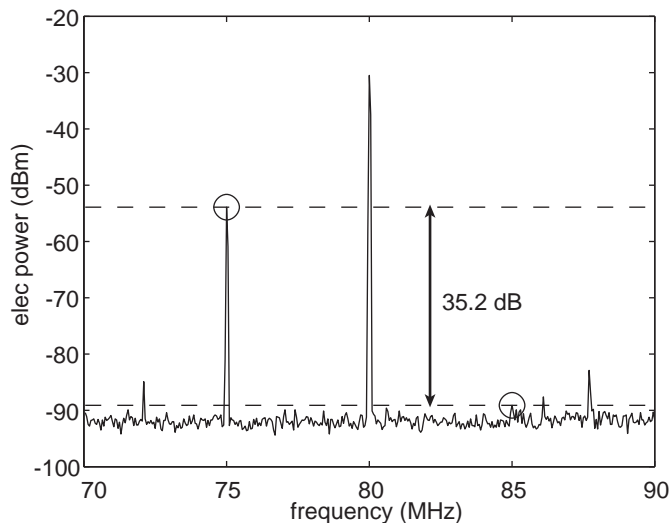


FIG. 5: A more detailed spectrum analyser trace of sideband suppression, with 35.2 dB difference between sidebands. Frequency lines at 72.1 MHz, 86.1 MHz and 87.7 MHz are from radio interference with the electronic equipment.

carrier (as measured by the heterodyne) is approximately 6 dB weaker than the sidebands.

We were especially careful to validate this heterodyne measurement of the carrier, because the directly detected power only dropped by 40 dB. The reason for this is that the majority of the residual carrier power was now in a higher-order, odd spatial mode (easily verified by looking at the intensity profile of the beam), which did not interfere efficiently with the heterodyne oscillator beam. The higher-order modes were thought to result from a spatially non-uniform polarisation of the light exiting the UTM which, when subsequently passed through a polarising beam splitter, produced modes reflecting the symmetry of the modulator. As such, for applications where spatial mode interference is important, the employment of a mode-cleaner cavity with free spectral range equal to the modulation frequency (or one of its integer divisors) should solve the problem.

In an attempt to confirm the variability of the UTM prototype, we endeavoured to map significant paths in the modulation parameter space. Fig. 6 and Fig. 7 show the result of sweeping through M-space in two cardinal directions: varying the relative phase between the two (constant amplitude) electrical signals; and varying the amplitude of one electrical signal while keeping the other signal amplitude, and the relative phase, constant. For matters of calibration, the UTM was initially set to the PM operating point (this initial state was used as the reference in labelling "in-phase" and "quadrature" components), and the relative gains and phases of the two double demodulation circuits were measured and factored out via correspondence with spectrum analyser data. The input polarisation was set to be elliptical with a vertical component slightly larger than the horizontal component. The results show that changing the

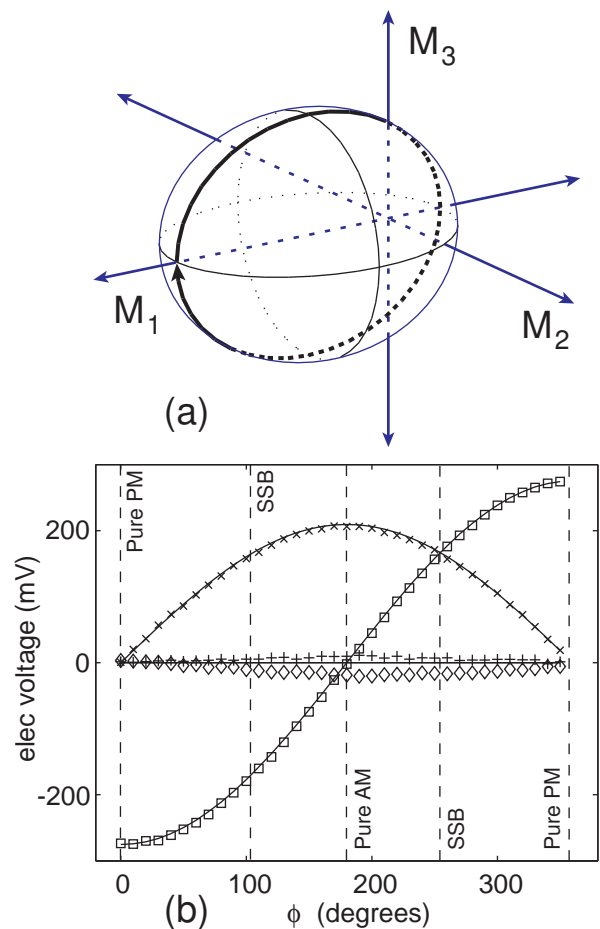


FIG. 6: (a) Modulation ellipse showing trajectory of measurement sweep through parameter space, where the phase difference between electrical signals, $\phi = \phi_1 - \phi_2$, is varied through 360° . (The ellipse has an (exaggerated) σ of $\approx 53^\circ$.) (b) Double-demodulation measurements of PM (squares and diamonds for in-phase and quadrature components respectively) and AM (pluses and crosses for in-phase and quadrature components respectively), with corresponding theoretical predictions (solid lines). The majority of modulation present is either PM or quadrature AM as predicted. This plot corresponds to $\sigma \approx 75^\circ$; a value derived by measuring, from corresponding spectrum analyser data, the phase ϕ at which the single sideband operating points occur. Using a result from Table I, the phase ϕ between the pure AM operating point and either of the single sideband operating points, is precisely equal to σ .

phase between the two electrical signals produces AM in quadrature to the original PM, whereas changing the amplitude of one electrical signal generates AM in-phase with the original PM. The data points are generally in good agreement with the theoretical predictions. Some small systematic errors are apparent, and are thought to be associated with unmatched electrical and optical impedances between the two crystals, and possibly to do with slightly unmatched optical power levels probing each crystal (ie a violation of our original assumption regarding polarisation states). Overall, the device is shown to be highly predictable, and that one can "dial-up" a particular modulation state on call, having calibrated the

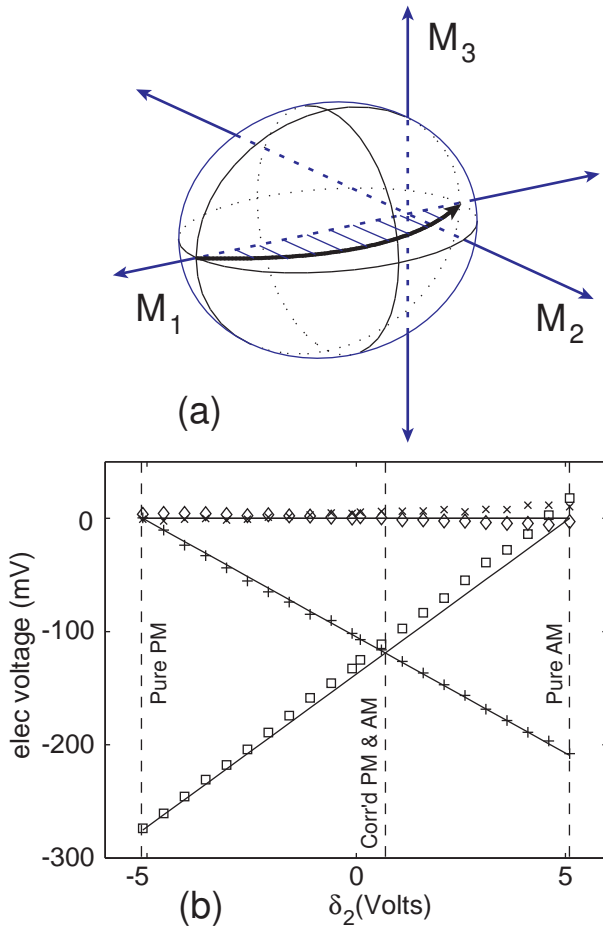


FIG. 7: (a) Modulation ellipse showing trajectory of measurement sweep through parameter space, where the strength of one electrical signal, δ_2 , is varied from +5.1 V to -5.1 V. The sweep involves varying the overall input electrical power, so the modulation trajectory does not stay on the ellipse surface, and instead traces out a parabolic curve. (The ellipse has an (exaggerated) σ of $\approx 53^\circ$.) (b) Double-demodulation measurements of PM (squares and diamonds for in-phase and quadrature components respectively) and AM (pluses and crosses for in-phase and quadrature components respectively), with corresponding theoretical predictions (solid lines). There is diverging agreement in the PM which may be caused by imperfectly matched electrical impedances for the two crystals. As in Fig. 6, the location of the correlated PM & AM point is shifted toward the pure AM point by about 0.7 V out of 5.1 V and, referring to Table II C, this corresponds to a value of $\sigma \approx 75^\circ$.

device initially.

It is instructive to notice that the cardinal operating points are not evenly spaced when sweeping across the parameter space. In particular, we see that the two single-sideband operating points are shifted toward the AM operating point in Fig. 6, and the correlated PM & AM operating point is similarly shifted in Fig. 7, relative to the perpendicular. This is a product of the non-circular polarisation of light input into the modulator device, and can be understood by reviewing the modulation ellipses in the two figures; the M_2 and M_3 axes intercept the ellipse at points that are closer to the AM operating

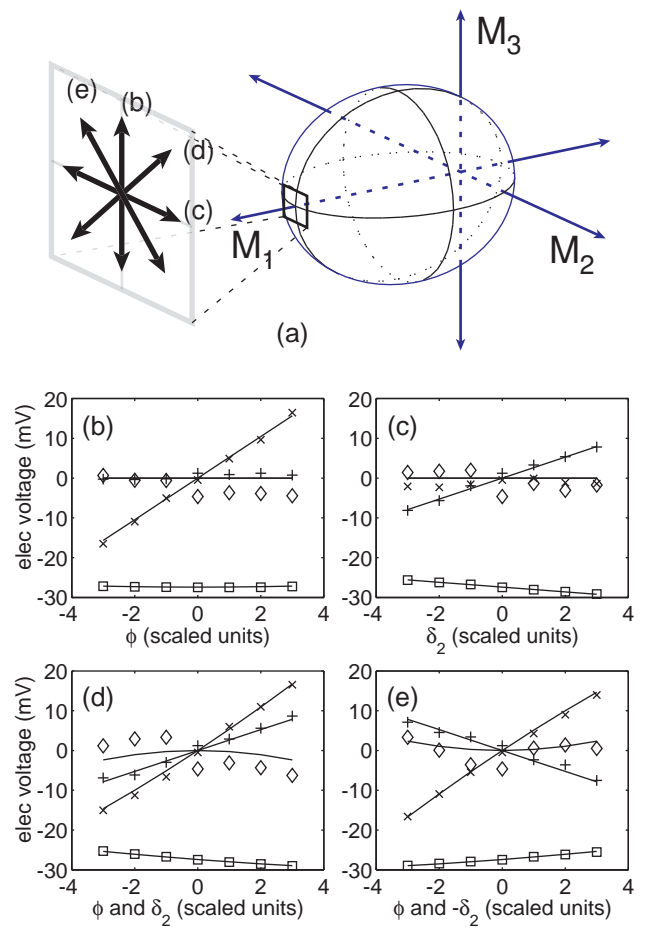


FIG. 8: (a) Modulation ellipse showing short-range trajectories designed to map local region near PM operating point. The electrical parameters $\phi = \phi_1 - \phi_2$ and δ_2 were varied to achieve these results, with units worth 5° and 0.44 V respectively. (b), (c), (d) and (e) show double-demodulation measurements of PM (squares and diamonds for in-phase and quadrature components respectively) and AM (pluses and crosses for in-phase and quadrature components respectively), with corresponding theoretical predictions (solid lines). Parameters varied were (b) ϕ , (c) δ_2 , (d) ϕ and δ_2 together with the same polarity, and (e) ϕ and $-\delta_2$ together with opposite polarities. *Note:* the in-phase PM data points (squares) have been scaled down by a factor of 10 to fit in the diagram. Also, the systematic error in the quadrature PM data is probably due to an electronic phase drift between signal generators, causing a small amount of in-phase PM data (which is an order of magnitude stronger) to couple across.

point than the PM. In fact, this provides us with a means of calibration of the relative transfer-function-amplitudes of the PM and AM double-demodulation circuits: they are set by assuring that (in Fig. 6) the PM and AM components are equal at the phase ϕ where the single sideband is known to occur (information which is obtained via comparison with spectrum analyser data). Also, by using the identities in Table I, we can derive a value of the polarisation parameter: $\sigma \approx 75^\circ$.

Fig. 8 shows scans of the local region near the PM operating point, with deviations in four directions. These data were taken with an offset locking application in

mind, as discussed earlier. The in-phase PM component (in-phase by definition) is by far the dominant signal, and has been scaled down by a factor of 10 to fit in the graphs. As expected, the UTM device can produce AM that is in-phase with the present PM, or AM that is in quadrature with the present PM, by changing the relative electrical signal amplitudes or phases respectively. In addition, both of these parameters can be varied together or oppositely, to give independent control over the two quadratures of AM resulting. We note that in the case of producing both in-phase and quadrature AM, a small component of quadrature PM appears (in other words, the phase of the PM changes, relative to that of the pure PM point used for the initial calibration). In actual fact, the quadrature PM data has a noticeably larger systematic error than the other three signals. This is most likely due to pollution from its in-phase counterpart, caused by the demodulation oscillator's phase drifting marginally (this was observed to happen even in spite of the electronic phase locking between signal generators).

A number of experimental difficulties deserve mentioning. As described in the context of the carrier suppression results, the UTM produced a spatially varying polarisation state, which produced a small percentage of higher-order spatial modes upon selecting out a polarisation component (of order 1% of the overall power). This interfered with our ability to directly measure the polarisation, which we did by measuring the overall detected power while rotating a diagnostic half-wave plate placed before the PBS. In this way, we measured a value of $\sigma \approx 70^\circ$ for the results shown in Figs. 6 to 8, as compared to $\sigma \approx 75^\circ$ measured by inference from spectrum analyser data. We assign a reasonably large error to the direct measurement value due to the presence of the higher-order spatial modes, and we favour measuring σ by inference from the data.

The overall optical path lengths of the modulating crystals were found to change significantly as they warmed up after starting the laser. The dual crystal design of the device goes a long way toward minimising this problem, and we have seen that the device is stable once it has warmed up. However, long term drift of the crystal lengths is possible, having a direct effect on the polarisation state leaving the device. We propose that, in circumstances where this becomes a problem, a feedback loop be employed to lock the polarisation state. A possible scheme would see the power level out of one PBS port monitored and used as a feedback signal (minus an offset equal to the desired power level) to the DC optical path length of one of the crystals, thus compensating for a mechanical path length change by feeding back to the refractive index.

Finally, the electrical impedances of the two crystals were not well matched for two reasons: the electronics were not identical; and the crystals themselves had "good" and "bad" spots which generated varying levels of modulation. In general terms, careful alignment can largely overcome this problem and return the two crystals

to an equal footing. The differing electrical impedances complicate the issue of generating a local oscillator with the phase-tracking property discussed earlier, since the voltages $V_{1,2}$ and modulation depths $\delta_{1,2}$ are not then related by the same factor. We submit that the device tested here is merely a prototype, and that careful management will suffice to deal with these issues as the need arises.

IV. CONCLUSION

We presented a thorough investigation, both theoretical and experimental, of a prototype Universally Tunable Modulator (UTM). The electrical-to-optical transfer function of the device was derived, both in terms of electrical and optical phasor notation, and using a geometric phase "Modulation Sphere" representation. Both pictures were shown to have merit, and a set of cardinal modulations were described in each notation. We reported on an experiment to characterise the prototype UTM, which involved using dual double-demodulation circuits to measure both AM and PM components simultaneously. Data sets were obtained and analysed to illustrate the variability and purity characteristics of the device; the device was shown to be highly predictable and capable of highly pure states. Applications for the UTM were discussed.

V. ACKNOWLEDGEMENTS

The authors are grateful to Russell Koehne for his skill and labour in modifying the original AM device. Stan Whitcomb thanks the gravitational wave research group at the Australian National University for their support and hospitality during his stay at the ANU.

This material is based on work supported by the Australian Research Council, and supported in part by the United States National Science Foundation under Cooperative Agreement No. PHY-0107417. This paper has been assigned LIGO Laboratory document number LIGO-P030031-00R.

APPENDIX A: APPENDICES

1. Derivation of UTM transfer function

This is an outline of the derivation of Eq. 3. First, we find the (more general) transfer function of the UTM when we allow the input beam to have any polarisation. At the end, we will simplify to the subcase described in the main text.

The input beam's polarisation will be characterised by two electric field phasor components, $\vec{L} = Le^{i\sigma_L}$ and $\vec{R} = Re^{i\sigma_R}$, as defined in a set of left-diagonal and right-diagonal spatial coordinate axes (with unit vectors \hat{L} and

\hat{R} respectively). The electric field exiting the UTM can be written as a vector (to include polarisation information) as:

$$\vec{E}_{\text{ExitingUTM}} = \left[\tilde{L} e^{i\Re\{\tilde{\delta}_1 e^{i\omega_m t}\}} \hat{L} + \tilde{R} e^{i\Re\{\tilde{\delta}_2 e^{i\omega_m t}\}} \hat{R} \right] e^{i\omega t}. \quad (\text{A1})$$

(From hereon in, we will suppress the $e^{i\omega t}$ term for the sake of brevity.) Upon passing through the vertically aligned linear polariser (equivalent to taking a dot product with the vector $(\hat{L} + \hat{R})/\sqrt{2}$), and expanding the complex exponentials to first order (hence assuming $|\tilde{\delta}_{1,2}| \ll 1$), the vertical electric field amplitude becomes:

$$E_{\text{OUT}} = \frac{1}{\sqrt{2}} \left[\tilde{L}(1 + i\Re\{\tilde{\delta}_1 e^{i\omega_m t}\}) + \tilde{R}(1 + i\Re\{\tilde{\delta}_2 e^{i\omega_m t}\}) \right]. \quad (\text{A2})$$

Next, we collect DC terms and oscillating terms, and factor out the overall optical phase:

$$E_{\text{OUT}} = \frac{\tilde{L} + \tilde{R}}{\sqrt{2}} \left[1 + \frac{i(|L^2 + \tilde{L}\tilde{R}^*|)}{|\tilde{L} + \tilde{R}|^2} \Re\{\tilde{\delta}_1 e^{i\omega_m t}\} + \frac{i(\tilde{R}\tilde{L}^* + R^2)}{|\tilde{L} + \tilde{R}|^2} \Re\{\tilde{\delta}_2 e^{i\omega_m t}\} \right]. \quad (\text{A3})$$

Now, we work to separate real and imaginary components for the oscillating terms:

$$E_{\text{OUT}} = \frac{\tilde{L} + \tilde{R}}{\sqrt{2}} \left[1 + \Re \left(\frac{\Im\{\tilde{R}\tilde{L}^*\}(\tilde{\delta}_1 - \tilde{\delta}_2)}{|\tilde{L} + \tilde{R}|^2} e^{i\omega_m t} \right) + i\Re \left(\frac{\Re\{\tilde{R}\tilde{L}^*\}(\tilde{\delta}_1 + \tilde{\delta}_2) + L^2\tilde{\delta}_1 + R^2\tilde{\delta}_2}{|\tilde{L} + \tilde{R}|^2} e^{i\omega_m t} \right) \right] \quad (\text{A4})$$

These real and imaginary oscillating terms correspond to AM and PM respectively, so we parameterize via:

$$E_{\text{OUT}} = \frac{|\tilde{L} + \tilde{R}|}{\sqrt{2}} + \Re\{\tilde{A}e^{i\omega_m t}\} + i\Re\{\tilde{P}e^{i\omega_m t}\} \quad (\text{A5})$$

with

$$\tilde{P} = \Re \left(\frac{\Re\{\tilde{R}\tilde{L}^*\}(\tilde{\delta}_1 + \tilde{\delta}_2) + L^2\tilde{\delta}_1 + R^2\tilde{\delta}_2}{\sqrt{2}|\tilde{L} + \tilde{R}|} \right) \\ \tilde{A} = \Re \left(\frac{\Im\{\tilde{R}\tilde{L}^*\}(\tilde{\delta}_1 - \tilde{\delta}_2)}{\sqrt{2}|\tilde{L} + \tilde{R}|} \right) \quad (\text{A6})$$

where the net optical phase shift has been discarded. Eqs. A5 and A6 constitute the general UTM transfer function for arbitrary input polarisation. Note that the PM component does not have the property of tracking the phase of the sum of the input electrical signals, since it generally depends on these inputs in different proportions. This is one of the reasons why we chose to restrict the polarisation to a subset.

If we choose said subset, $L = R = E_{\text{IN}}/\sqrt{2}$ (equal power in the two polarisation axes), and define $\sigma =$

$\sigma_R - \sigma_L$ as the phase between the two polarisation components, then the equations reduce to:

$$E_{\text{OUT}} = E_{\text{IN}} \cos\left(\frac{\sigma}{2}\right) + \Re\{\tilde{A}e^{i\omega_m t}\} + i\Re\{\tilde{P}e^{i\omega_m t}\} \quad (\text{A7})$$

and

$$\tilde{P} = \frac{E_{\text{IN}}}{2} \cos\left(\frac{\sigma}{2}\right) (\tilde{\delta}_1 + \tilde{\delta}_2) \\ \tilde{A} = \frac{E_{\text{IN}}}{2} \sin\left(\frac{\sigma}{2}\right) (\tilde{\delta}_1 - \tilde{\delta}_2). \quad (\text{A8})$$

Eqs. 2 and 3 in the text are the same as these, but with a dimensionless definition of \tilde{P} and \tilde{A} .

2. Derivation of UTM transfer function for Q-space and M-space parameters

This is an outline of the derivation of Eq. 8. As with Appendix A 1, we derive the Q-space to M-space transfer function of the UTM for any input light polarisation state. At the end, we reduce the equations to the case where the allowed polarisations are restricted. The derivation consists of transforming parameters \tilde{P} and \tilde{A} to M-space parameters (M_1, M_2, M_3) using Eq. 6, and transforming parameters $\tilde{\delta}_1$ and $\tilde{\delta}_2$ to Q-space parameters (Q_1, Q_2, Q_3) using Eq. 7, and hence converting Eq. A6 from one set of coordinates to another.

Firstly, it is convenient to write down a few intermediate terms using Eq. A6 as a starting point. We also convert to Q-space parameters (via Eq. 7) as we go.

$$P^2 = \tilde{P}^* \tilde{P} = \frac{\Re\{\tilde{R}\tilde{L}^*\}^2 [Q_0 + Q_2] + 2L^2 R^2 Q_2}{2|\tilde{L} + \tilde{R}|^2} + \frac{\frac{1}{2}[(L^4 + R^4)Q_0 + (L^4 - R^4)Q_1]}{2|\tilde{L} + \tilde{R}|^2} + \frac{\Re\{\tilde{R}\tilde{L}^*\}[(L^2 + R^2)Q_0 + (L^2 - R^2)Q_1 + (L^2 + R^2)Q_2]}{2|\tilde{L} + \tilde{R}|^2} \quad (\text{A9})$$

$$A^2 = \tilde{A}^* \tilde{A} = \frac{\Im\{\tilde{R}\tilde{L}^*\}^2 [Q_0 - Q_2]}{2|\tilde{L} + \tilde{R}|^2} \quad (\text{A10})$$

$$\Re\{\tilde{P}\tilde{A}^*\} = \frac{\Re\{\tilde{R}\tilde{L}^*\}\Im\{\tilde{R}\tilde{L}^*\}Q_1}{2|\tilde{L} + \tilde{R}|^2} + \frac{\frac{1}{2}\Im\{\tilde{R}\tilde{L}^*\}[(L^2 - R^2)Q_0 + (L^2 + R^2)Q_1 - (L^2 - R^2)Q_2]}{2|\tilde{L} + \tilde{R}|^2} \quad (\text{A11})$$

$$\Im\{\tilde{P}\tilde{A}^*\} = \frac{-\Im\{\tilde{R}\tilde{L}^*\}[\Re\{\tilde{R}\tilde{L}^*\} + \frac{1}{2}(L^2 + R^2)]Q_3}{2|\tilde{L} + \tilde{R}|^2} \quad (\text{A12})$$

Things can be simplified somewhat by using a Stokes' parameter representation for the polarisation from this

point. Here, we (unusually) define the Stokes' parameters in terms of left-diagonal and right-diagonal electric field components (equivalent to rotating the usual X-Y axes anti-clockwise by 45°):

$$\begin{aligned} S_0 &= R^2 + L^2 \\ S_1 &= R^2 - L^2 \\ S_2 &= 2RL\cos(\sigma) = 2\Re\{\tilde{R}\tilde{L}^*\} \\ S_3 &= 2RL\sin(\sigma) = 2\Im\{\tilde{R}\tilde{L}^*\} \end{aligned} \quad (\text{A13})$$

when the previous four equations become:

$$\begin{aligned} P^2 &= \frac{1}{4} [S_0 Q_0 - S_1 Q_1 + S_2 Q_2 \\ &\quad - \frac{S_3^2}{2(S_0 + S_2)} (Q_0 - Q_2)] \\ A^2 &= \frac{1}{8} \frac{S_3^2}{S_0 + S_2} (Q_0 - Q_2) \\ \Re\{\tilde{P}\tilde{A}^*\} &= \frac{1}{8} \left[S_3 Q_1 - \frac{S_3 S_1}{S_0 + S_2} (Q_0 - Q_2) \right] \\ \Im\{\tilde{P}\tilde{A}^*\} &= -\frac{1}{8} S_3 Q_3 \end{aligned} \quad (\text{A14})$$

These intermediate quantities are then converted to M-space parameters (via Eq. 6). We write the result here in matrix form:

$$\begin{bmatrix} M_0 \\ M_1 \\ M_2 \\ M_3 \end{bmatrix} = \frac{1}{4} \begin{bmatrix} S_0 & -S_1 & S_2 & 0 \\ S_2 + \frac{S_3^2}{S_0 + S_2} & -S_1 & S_0 - \frac{S_3^2}{S_0 + S_2} & 0 \\ \frac{-S_1 S_3}{S_0 + S_2} & S_3 & \frac{S_1 S_3}{S_0 + S_2} & 0 \\ 0 & 0 & 0 & -S_3 \end{bmatrix} \begin{bmatrix} Q_0 \\ Q_1 \\ Q_2 \\ Q_3 \end{bmatrix} \quad (\text{A15})$$

Eq. A15 is the general Q-space to M-space transfer function for the UTM with any input polarisation. It gives further insight into the manner in which choosing $L \neq R$ affects the properties of the system. The parameters M_1 and M_2 depend on both Q_1 and Q_2 , which means that a sphere in Q-space will be distorted in the M_1 - M_2 plane by the transformation. The resulting surface is an ellipsoid whose major axis is no longer collinear with the M_1 -axis, but is at an angle subtended in the M_1 - M_2 plane. This distortion certainly interferes with most of the favourable properties of the system. For example, none of the poles of the ellipse coincide with a coordinate axis, making any of the six operating points discussed more complicated to find.

The restriction on polarisation states discussed in the text is equivalent to setting S_1 to zero (which in turn forces $S_0 = E_{\text{IN}}^2$, $S_2 = E_{\text{IN}}^2 \cos(\sigma)$ and $S_3 = E_{\text{IN}}^2 \sin(\sigma)$), when Eq. A15 reduces to:

$$\begin{bmatrix} M_0 \\ M_1 \\ M_2 \\ M_3 \end{bmatrix} = \frac{E_{\text{IN}}^2}{4} \begin{bmatrix} 1 & 0 & \cos(\sigma) & 0 \\ \cos(\sigma) & 0 & 1 & 0 \\ 0 & \sin(\sigma) & 0 & 0 \\ 0 & 0 & 0 & -\sin(\sigma) \end{bmatrix} \begin{bmatrix} Q_0 \\ Q_1 \\ Q_2 \\ Q_3 \end{bmatrix} \quad (\text{A16})$$

Once again, Eq. 8 from the text is the dimensionless equivalent of this, where E_{IN} is external to the definition of the M-space parameters.

-
- [1] B. Davies and J. Conradi, IEEE Phot. Tech. Lett. **10**, 600-602 (1998).
- [2] G. Smith, D. Novak, and Z. Ahmed, Elec. Lett. **33**, 74-75 (1997)
- [3] R. W. P. Drever, J. L. Hall, F. V. Kowalski, J. Hough, G. M. Ford, A. J. Munley, and H. Ward, Appl. Phys. B **31**, 97 (1993)
- [4] L. Schnupp, Conference Presentation, in *European collaboration Meeting on Interferometric Detection of Gravitational Waves* (1988)
- [5] LIGO Scientific Collaboration, Ed. P. Fritschel "Advanced LIGO Systems Design" *LIGO Technical Note T010075* (2001) <http://antares.ligo.caltech.edu/dcc/default.htm>
- [6] J. Mizuno, K. A. Strain, P. G. Nelson, J. M. Chen, R. Schilling, A. Rudiger, W. Winkler, and K. Danzmann, "Resonant sideband extraction: a new configuration for interferometric gravitational wave detectors", Phys. Lett. A **175**, 273-276 (1993)
- [7] K. A. Strain and J. Hough, "Experimental Demonstration of the use of a Fabry-Perot cavity as a mirror of variable reflectivity", Rev. Sci. Instrum. **64** (1994)
- [8] G. de Vine, D. A. Shaddock, and D. E. McClelland, "Experimental Demonstration of variable reflectivity signal recycling for interferometric gravitational wave detectors", Opt. Lett. **27**, 1507-1509 (2002)
- [9] A. Loayssa, C. Lim, A. Nirmalathas, and D. Benito, Elec. Lett. **39**, 97 (2003)
- [10] K. Yonenaga and N. Takachio, IEEE Phot. Tech. Lett. **5**, 949-951 (1993)
- [11] See, for example: A. Loayssa, D. Benito, and M. J. Garde, IEEE Phot. Tech. Lett. **13**, 869-971 (2001); S. Shimotsu, S. Oikawa, T. Saitou, N. Mitsugi, K. Kubodera, T. Kawanishi, and M. Izutsu, IEEE Phot. Tech. Lett. **13**, 364-366 (2001)
- [12] F. Grosshans, G. V. Assche, J. Wenger, R. Brouri, N. J. Cerf, and Ph. Grangier, Nature **421**, 238 (2003)
- [13] See, for example, W. P. Bowen, N. Treps, B. C. Buchler, R. Schnabel, T. C. Ralph, H.-A. Bachor, T. Symul, and P. K. Lam, Phys. Rev. A **67**, 032302 (2003) or A. Furusawa, J. L. Sorensen, S. L. Braunstein, C. A. Fuchs, H. J. Kimble, and E. S. Polzik, Science **282**, 706 (1998).
- [14] G. G. Stokes, Trans. Camb. Phil. Soc. **9**, 399 (1852).